MS# 5906_Revision 1

Apatite in the dike-gabbro transition zone of mid-ocean ridge: Evidence for brine assimilation by axial melt lens

CHAO ZHANG, JUERGEN KOEPKE, MORITZ ALBRECHT, INGO HORN, FRANCOIS HOLTZ

Institut für Mineralogie, Leibniz Universität Hannover, 30167 Hannover, Germany
Corresponding author: Chao Zhang.
Telephone: +49 (0)511 762-5280. Fax: +49 (0) 511 762-3045.
Email: c.zhang@mineralogie.uni-hannover.de

ABSTRACT

We present textures and halogen and trace-element compositions of apatites in intrusive rocks from the dike-gabbro transition zone of a fast-spreading mid-ocean ridge, which was formed at the East Pacific Rise and recently drilled by IODP Hole 1256D. These data are used to discuss the properties of parental magmas and seawater-derived hydrothermal fluids at the roof of the axial melt lens during the formation of oceanic crust. In general, zoning of apatites from three different lithologies, tonalites, diorites and gabbros, is common and shows a consistent evolution trend with depletion in Cl and REEs from core to rim. The cores are usually homogenous in composition and interpreted as magmatic origin, whereas zones with lower Cl and REEs are disseminated with heterogeneous concentrations, indicating exchanges with hydrothermal fluids. The apatite cores in tonalites are rich in both F and Cl, with $X_{\mathrm{Ap}}^{\mathrm{F}}$ (proportion of fluorapatite endmember) up to 0.5 and $X_{\mathrm{Ap}}^{\mathrm{Cl}}$ (proportion of chlorapatite endmember) up to 0.4. In contrast, the apatite cores in gabbros have high $X_{\mathrm{Ap}}^{\mathrm{Cl}}$ (up to 0.85) and very low X_{Ap}^{F} (<0.05). The two contrasting types of apatite cores are both observed in diorites, implying that magma mixing processes may have controlled the formation of the dioritic intrusives. The strong depletions in Cl and $\mathrm{REE_S}$ in some parts of the apatite crystals (mainly rim) can be explained by removal of these components via hydrothermal fluids. Based on available F-Cl-OH exchange coefficients for apatite-melt, the very high Cl/OH and Cl/F ratios and high Cl contents calculated for tonalitic melts cannot be reconciled with a formation of these felsic melts by partial melting of amphibole-bearing metabasalts, but indicate that an assimilation of high-Cl brines must have

29 occurred. Similarly, the low-F chlorapatites in gabbros also imply an assimilation of high-Cl
30 brines. The source of high-Cl fluids in the axial magmatic system may result from seawater-
31 derived fluids, which may form immiscible vapor and brine at high temperatures as a result of
32 hydrothermal boiling.

33 ## INTRODUCTION

34 At mid-ocean ridges (MORs), hydrothermal circulations and fluid-rock interactions within
35 oceanic crust have various patterns and lead to the formation of various products at different
36 crustal levels (Alt, 1995). At fast-spreading ridges, axial melt lens (AML) serves as a critical
37 layer for the crustal accretion (Kent et al., 1990), which involves various processes resulting in
38 magma transport and heat loss (Phipps Morgan and Chen, 1993; Coogan, 2014). The AML is a
39 dynamic magma chamber that inflates and shrinks temporally, and is controlled by periodic
40 replenishment of magma (Rannou et al., 2006; Colman et al., 2012) as well as cooling and
41 crystallization at the roof (Maclennan et al., 2005; Zhang et al., 2014). At the roof of the AML,
42 dynamic movement of the boundary between the magma body and overlying sheeted dikes
43 results in intense melt-rock interactions, which account for contact metamorphism and partial
44 melting of the overlying crustal rocks (Gillis, 2008; Koepke et al., 2008; Zhang et al., 2014;
45 Erdmann et al., 2015). In such circumstances, assimilation of these materials into the basaltic
46 magmas of the AML is regarded as plausible and important in modifying the compositions of
47 MOR basalts (e.g. Coogan et al., 2003; France et al., 2014). Cl over-enrichments in erupted lavas
48 and melt inclusions at MORs, which cannot be fully explained by fractional crystallization, have
49 been considered as important evidence for pre-eruption assimilation of high-Cl contaminants in
50 the magmatic system (Michael and Schilling, 1989; Wanless et al., 2010; Freund et al., 2013;
51 Kendrick et al., 2013). In addition, there are also several observations from gabbroic intrusive
52 rocks, which are part of the solidified AML, providing direct evidence of assimilation processes.
53 For example, the Cl contents of magmatic amphiboles in gabbros at Hess Deep (East Pacific Rise,
54 fast-spreading ridge) are >10 times higher than that in magmatic amphiboles that occur at the
55 Mid-Atlantic Ridge (slow-spreading ridge), clearly supporting the idea that the AML under fast-
56 spreading ridges is an ideal place for efficient assimilation (Coogan et al., 2001; Gillis et al.,
57 2003).

The Integrated Ocean Drilling Program (IODP) Hole 1256D at the East Pacific Rise, for the first time, penetrated and sampled the dike-gabbro transition zone of an intact oceanic crust (Wilson et al., 2006; Teagle et al., 2012), and thus provided an invaluable chance to study the magmatic and hydrothermal processes in the AML. Detailed observations on the dike-gabbro transition zone (Koepke et al., 2008; Koepke et al., 2011), whole-rock geochemical data (Zhang et al. submitted to Journal of Petrology) and dedicated experimental studies (France et al., 2010; Erdmann et al., 2015) indicate that the products of hydrous partial melting of the sheeted dikes overlying the gabbros, i.e. small amount of felsic melts, are the most likely contaminants to be assimilated by the AML magma system. Tonalitic veins intruding gabbros and sheeted dikes have also been observed from the core drilling (Teagle et al., 2012). The assumed protoliths of the felsic melts, i.e. sheeted dikes, have been hydrothermally altered with ingress of seawater-derived fluids. This may account for the high Cl contents (1000-3000 ppm) in the amphiboles of the pyroxene hornfels that represent the melting residue phase (Koepke et al., 2008).

Estimation of the cooling rate of the pyroxene hornfels suggests that there should be multiple events of hydrothermal alteration in-between hydrous partial melting events (Zhang et al., 2014), during which amphiboles consumed in the previous partial melting event can be formed again as products of the following hydrothermal alteration events. In such cases, it might be difficult to use whole-rock data of commonly used geochemical tracers (such as boron and chlorine) for tracking fluid-relevant processes in the AML. The latest high-temperature alteration accompanying the solidification of the AML (Zhang et al., 2014) may have blurred the composition of the plutonic rocks, especially at locations near the dike-gabbro boundaries where Sr isotopes indicate the strongest alteration (Harris et al., 2015). Although general models for cycling of hydrothermal fluid throughout the oceanic crust have been constructed (Fontaine et al., 2007; Alt et al., 2010), the evolution of fluid properties (e.g. salinity), associated with the interaction with the AML (Nehlig, 1993), especially at high temperatures, is still poorly understood. A possible tracer mineral for such activities is apatite, which is ubiquitous in the plutonic rocks at the dike-gabbro transition zone, and which may provide insights into both the magmatic stages and hydrothermal alteration processes (Harlov, 2015; Webster and Piccoli, 2015). Particularly, because of the slow rate of intra-crystal diffusion of anions and cations (Brenan, 1994; Cherniak, 2000; Hughes, 2015), apatite zoning is common and retains the records of the changing melt and/or fluid compositions that have been locally in equilibrium with the

apatite. In this paper, we present data on the texture and composition of apatites in the intrusive rocks drilled from IODP Hole 1256D. Implications for the properties of seawater-derived fluid and its role in the formation of magmatic chlorapatite and in the post-magmatic hydrothermal metasomatism will be discussed.

SAMPLES FROM IODP HOLE 1256D

The samples of this study are drilled cores from IODP Hole 1256D (6°44.2'N, 91°56.1'W), which were formed at the East Pacific Rise during superfast spreading and is now located in the 15-Ma old oceanic lithosphere of the Cocos plate (Fig. 1). The drilling has penetrated a total depth of 1521.6 meters below seafloor (mbsf), and two gabbroic intrusions have been encountered at depths of 1405-1460 mbsf and 1480-1495 mbsf, respectively (Teagle et al., 2006; Koepke et al., 2011; Teagle et al., 2012). Some more felsic lithologies, such as gabbronorite, diorite and tonalite, are closely associated with the gabbroic intrusions. Whole-rock geochemical data indicate that the gabbros and gabbronorites have similarly high Mg# [100×molar Mg/(Mg+Fe); 55-70] and might be compositionally close to the parental magma of the erupted lavas (Fig. 2). In contrast, the diorites and tonalites, characterized by much lower Mg# (ca. 30), potentially represent more evolved magmas derived from basaltic parental magmas or partial melts of the altered sheeted dikes, or even a mixture of both end-members. In this study, twelve typical samples (see Supplementary Table 1 for IODP core information), with emphases on felsic lithologies, have been selected for detailed in-situ micro-analyses on apatite. Seven samples were collected from depths close to the shallower gabbroic intrusion, including a veined tonalite (212-1-P6), a massive tonalite (214-1-P14), a massive diorite (214-1-P10, 217-1-P21), a patch diorite (214-2-P10, see Fig. 3a), and two gabbros (214-1-P27, 216-1-P13). Another five samples were collected from depths close to the deeper gabbroic intrusion, including three massive diorites (230-1-P5, R14-A, R17), a gabbro (232-2-P1) and a tonalite vein (235-1-P5). Sample 214-2-P10 shows interconnected dioritic patches within gabbro matrix (Fig. 3a), illustrating a gradual chemical transition at the boundary of these two domains where amphibole usually replaces clinopyroxene. Both samples 214-1-P14 (tonalite) and 214-1-P10 (diorite) show intrusive boundaries with surrounding gabbros, while samples 230-1-P5 (diorite) and R14-A (diorite) are influenced by contact with pyroxene hornfels (i.e. a contact metamorphism product of the

sheeted dike). In addition, tonalites usually occur as veins intruding other lithologies, such as pyroxene hornfels (e.g. sample 212-1-P6) or diorite (sample 235-1-P5, see Fig. 3b). In all apatite-bearing lithologies, apatites are usually associated with actinolite, albite and quartz (see below).

METHODS

Electron probe microanalyses (EPMA)

Major and minor elements of apatites were analyzed using a Cameca SX100 electron microprobe equipped with 5 spectrometers and an operating system "Peak sight" at the Institute of Mineralogy, Leibniz University of Hannover, Germany. The materials for calibration include synthetic oxides (Fe, Mn), wollastonite (Si, Ca), albite (Na), fluorapatite (P, F), halite (Cl), pyrite (S). The fluorapatite crystal used here is the well-known reference Durango apatite (USNM 104021), and the homogeneity of the same crystal has been confirmed by a detailed test of Marks et al. (2012). Raw analytical data were corrected using the standard PAP procedures (Pouchou & Pichoir, 1991). The acceleration voltage was set as 15 kV. In order to avoid the variations of F and Cl X-ray count rates during analysis (Stormer et al., 1993; Goldoff et al., 2012), we used a defocused beam of 10 μm (5 μm in a few cases) and a beam current of 10 nA for analyzing F and Cl. Analyses were preferentially performed on apatite sections with a crystallographic orientation nearly parallel to the *c*-axis (i.e., the *c*-axis being perpendicular to the electron beam). A similar method and dedicated tests using the same equipments have been reported in Zhang et al. (2012), which confirms the importance of the crystallographic orientation in the analysis of halogens in apatite described in Stormer et al. (1993) and Goldoff et al. (2012). We used LPET and PC1 as diffraction crystals for Cl and F, respectively. Analyses on the Durango apatite (USNM 104021) yielded 3.32±0.14 (2sd) wt% F, 0.42±0.02 (2sd) wt% Cl and 0.33±0.08 (2sd) wt% SO_3, which were in good agreement with the recommended values: F ~3.53 wt %, Cl ~0.41 wt %, and SO_3 ~0.38 wt% (Young et al., 1969; Marks et al., 2012). For measuring F in amphibole, we applied the EMPA method of Zhang et al. (2015) that takes into account the potential spectral interferences of F*K*α, Fe*L*α and Mg*K*β lines when using a W-Si multilayered pseudocrystal as diffraction crystal. Considering the general formula of apatite to be $M_5(TO_4)_3X$, (M = Ca, Fe, Mn,

Na; T = P, Si, S; X = OH, F, Cl), the structure calculation has been performed on the basis of M+T = 8. The molar proportion of the endmembers hydroxylapatite ($X_{\mathrm{Ap}}^{\mathrm{OH}}$), fluorapatite ($X_{\mathrm{Ap}}^{\mathrm{F}}$) and chlorapatite ($X_{\mathrm{Ap}}^{\mathrm{Cl}}$) has been calculated assuming $X_{\mathrm{Ap}}^{\mathrm{OH}}+X_{\mathrm{Ap}}^{\mathrm{F}}+X_{\mathrm{Ap}}^{\mathrm{Cl}} = 1$ (see Supplementary Table 2 for EMPA data and results of formula calculation).

Laser-ablation coupled Inductively Coupled Plasma-Mass Spectrometry (LA-ICP-MS)

Trace elements concentrations in apatites were measured on polished thin sections, using a LA-ICP-MS facility at the Institute of Mineralogy, Leibniz University of Hannover. The LA system was build in-house based on a Spectra-Physics™ Solctice femtosecond (fs) laser operating in the deep UV at 194 nm. The regenerative amplified system is pumped with 500 Hz yielding a pulse energy of 70 μJ at a wavelength of 194 nm. For analyses, a constant repetition rate of 10 Hz was used. Thin sections were ablated by laser pulses with a spot size of 12-20 μm, using the raster mode or s spot mode dependent on the compositional homogeneity in terms of F and Cl (determined by X-ray mapping with EPMA). The ablation system, sample cell and operational conditions have been described in detail by Horn et al. (2006) using an older fs-laser system. The ablated sample particles were transported by helium gas flow through the cell and are subsequently mixed with argon prior to entering the plasma torch. The elemental analyses were conducted using an Element XR fast scanning sector field ICP-MS (ThermoScientific™) working in the fast mode with a sweep time of 1.49 s for scanning 40 isotopes. The data were acquired on five sample lines in the peak center with 4 ms sample time, which resulted in a dwell time of 20 ms per element. Spectroscopic interference from oxide formation was monitored by measuring the ThO/Th ratio during machine tuning, which was less than 0.2 %. Signal collection for each analysis was performed with an overall time of 180 sec, including ~80 sec for background (laser off) and ~100 sec for signal integration (laser on). The CaO content determined by EPMA was used as internal standard (^{43}Ca), and quantification was performed based on the NIST SRM 610 reference glass (Pearce et al., 1997). The BCR-2G basalt glass was measured periodically as an external reference for quality control and overall analytical stability. The reproducibility was better than 5% for all analyzed elemental concentrations. Raw data were processed using the SILLS software package (Guillong et al., 2008). Because Sr, Y and the rare earth elements (REEs) are the trace elements with highest concentrations in the analyzed apatites

comprise the most abundance of trace elements in analyzed apatites, only these elements are listed (Supplementary Table 3) and are used in discussion.

RESULTS

Textures of apatite

Tonalite. The apatites in tonalites are usually euhedral to subhedral prismatic, occurring along grain boundaries of quartz, albite, actinolite and magnetite (Fig. 4). The length of apatites varies within 100-500 μm. As revealed by back-scattered electron (BSE) images and mapping with Ca Kα, Cl Kα and F Kα spectral lines, all studied apatites show strong zoning. The zoning is composed of a primary part (core) and secondary zones (mostly rim). Compared to the primary part, the secondary zones are characterized by abundant dark holes, lower brightness in BSE (indicating depletion in heavy trace elements), depletion in Cl and enrichment in F. The replaced zones may occur as regular rim surrounding the core (Fig. 4a), and as irregular patches and veins invading the grains (Fig. 4b). Observations on apatites with different crystallographic orientations reveal that the secondary apatite is more abundant parallel to the *c*-axis than along other directions.

Diorite. The apatites in diorites show similar features as those in the tonalites. They coexist commonly with actinolite, chlorite, quartz, plagioclase and albite, and show an euhedral prismatic habit, as well as low-Cl secondary zones surrounding or invading high-Cl primary parts (Fig. 5). At least two secondary generations can be observed in some minerals (Fig.5), showing pronounced depletion in Cl with time. Tiny magnetite crystals may occur as inclusions in apatite, but are not in particular associated with the secondary zones (Fig. 5a). Apatites enclosed in actinolite show a large proportion of patchy secondary zones but also strongly irregular rims (Fig. 5b).

Gabbro. The apatites in gabbros also contain a high proportion of grains that show a strong chemical exchange when compared to the original parts. Several secondary generations can be distinguished, and the chemical variation is characterized by a significant depletion in Cl but very weak or no enrichment in F compared to the cores (Fig. 6). In contrast to those in tonalites

and diorites, the apatites in gabbros usually show anhedral habit and irregular crystal boundary. Similar to some apatites in diorites, strongly irregular crystal boundaries can be observed (Fig. 6a). Some apatites, which are associated with large magnetite (and ilmenite lamellae exsolution), titanite and pyrite (Fig. 6b), show an absence of cores and heterogeneous compositions in the whole crystal (e.g. Cl and F revealed by mapping).

Summary on textures. In general, an original Cl-rich homogenous part can be observed for most apatite crystals. The interfaces between cores and secondary zones are usually sharp as indicated by BSE and EPMA mapping for Cl and F. This in turn indicates that the secondary zone was resulting from dissolution and reprecipitation (Tacker and Stormer, 1989; Boudreau and McCallum, 1990; Harlov et al., 2002; Harlov et al., 2005; Wang et al., 2014). Thus, the secondary zones are replacements over precursor cores (see more discussion in section "Metasomatic apatite and implications for hydrothermal fluids"). Solid-state inter-diffusion between replaced and precursor zones seems insignificant as indicated by the strong compositional contrast between them, which may reflect the important effects of pressure and temperature on the diffusivities of F, Cl and OH in apatite (Brenan, 1994). The inter-diffusion between hydrothermally replaced rims and precursor cores is expected at a low pressure (500 bar) and a low temperature (<400 °C), and expected size that can be affected by such inter-diffusion is extremely short (Brenan, 1994). Epitaxial growth along low-Cl zones has not been observed for any of the studied apatite crystals. Other REE-rich minerals, such as monazite or xenotime, are absent in both the original parts and the replaced zones. All these features indicate that the fluids played an important role in the exchange mechanisms affecting the apatite grains. Compared to melt-solid systems, replacement reactions in fluid-solid systems are much more effectively responsible for such replacement (Putnis and John, 2010), implying the important role of fluids in the formation of the low-Cl parts (Figs. 4-6). In addition, the replaced Cl-poor zones are characterized by a pervasive porosity (i.e. dark holes in BSE), which can serve as channels for material transport during hydrothermal replacement (Yanagisawa et al., 1999; Kusebauch et al., 2015).

Halogen distribution in primary apatites

Although the apatites have a very wide compositional range in terms of Cl and F (Fig. 7), the

compositional field of apatite cores is much more restricted. These cores are interpreted to represent primary compositions of apatites that crystallized at a magmatic stage. Based on compositional features, two types of apatite cores can be clearly identified, i.e. high-Cl fluorapatite ($X_{\mathrm{Ap}}^{\mathrm{F}}$ ~0.6, $X_{\mathrm{Ap}}^{\mathrm{Cl}}$ ~0.3) and low-F chlorapatite ($X_{\mathrm{Ap}}^{\mathrm{F}}$ ~0.1, $X_{\mathrm{Ap}}^{\mathrm{Cl}}$ ~0.6). The two different compositional fields are marked in Fig. 7. In gabbros, apatites have a very restricted compositional range with Cl contents of ~5.5 wt% and $X_{\mathrm{Ap}}^{\mathrm{Cl}}$ of ~0.83. The high-Cl fluorapatite cores are observed only in diorites and tonalites, whereas the low-F chlorapatites are observed only in gabbros and diorites. Thus, only apatite cores from the diorites can occur within the two compositional fields. It is also interesting to note that intermediate apatite compositions (i.e., compositions in between the two grey fields in Fig. 7) were not observed in the diorites. It is emphasized that the Cl concentrations observed in the primary apatites are very high, which have been rarely reported in terrestrial magmatic systems (Piccoli and Candela, 2002; Webster and Piccoli, 2015).

Halogen distribution in secondary apatites

The compositional field of the apatites affected by secondary processes, which can be clearly identified from textural observations (see above), is very large compared to the primary apatites (Fig. 7). When compared to the primary compositions, some main variation trends can be observed. In the gabbros, the secondary apatites show a continuous Cl-decreasing trend starting from $X_{\mathrm{Ap}}^{\mathrm{Cl}}$ of ~0.6 towards an OH-Ap end-member. In some apatites from the gabbros, it can be noted that the secondary process was also accompanied by an increase in F content in the apatite (Fig. 7b). In the tonalite, most secondary apatites show a general increase of the OH-Ap component at the expense of $X_{\mathrm{Ap}}^{\mathrm{F}}$ and $X_{\mathrm{Ap}}^{\mathrm{Cl}}$. However, a detailed observation shows that different variation trends can be noted and that two boundary conditions can be identified: on one hand, there is a pronounced Cl-decreasing trend starting from the low-F primary chlorapatite and ending with $X_{\mathrm{Ap}}^{\mathrm{Cl}}$ of ~0.03, at nearly constant ratio of $X_{\mathrm{Ap}}^{\mathrm{F}}$; on the other hand, some apatites show an increase of $X_{\mathrm{Ap}}^{\mathrm{Cl}}$ at nearly constant OH content. These two differing variation trends are further discussed in the next section. As a result of the complex variations observed in gabbros and diorites, the secondary apatites from the diorite cover the whole compositional field observed for gabbros and tonalites, with two possible primary apatite compositions.

Trace element distribution in apatites

The SiO_2, FeO and Na_2O contents are within the same range of apatites for tonalites, diorites and gabbros with concentrations of ≤0.55 wt% SiO_2, ≤0.50 wt% FeO and ~0.20 wt% Na_2O (EPMA data, see Supplementary Table 2). The minerals also contain 60-180 ppm Sr, 800-2800 ppm Y and ∑REE varies in the range 1800-6000 ppm (LA-ICP-MS data, see Supplementary Table 3). The REE patterns (normalized to chondrite, data from Sun and McDonough, 1989) are shown in Fig. 8. In all analyses, a negative Eu anomaly can be observed. The highest REE concentrations are observed from the primary apatites, and the secondary apatites have systematically lower REE concentrations. In the gabbros, there is a more pronounced depletion in lightest REEs (La and Ce) and heaviest REEs (Yb and Lu) in apatite. Therefore $(La/Sm)_N$ (N means normalization to chondrite) and $(Lu/Gd)_N$ ratios tend to decrease with decreasing ∑REE (Fig. 8c).

DISCUSSION AND IMPLICATIONS

Metasomatic apatite and implications for hydrothermal fluids

As indicated by the textures and covariation of REE vs. Cl, it is clear that REEs are removed from the apatite structure with advancing replacement. Several charge-compensating substitution mechanisms have been proposed for the incorporation or removal of trivalent Y and REEs in apatites (Pan and Fleet, 2002), and the following two may be the most important ones:

$$Ca^{2+} + PO_4^{3-} \leftrightarrow SiO_4^{4-} + (Y, REE)^{3+} \quad (1)$$

$$2\ Ca^{2+} \leftrightarrow Na^{+} + (Y, REE)^{3+} \quad (2)$$

These two mechanisms are supported by the plot of Y+REEs vs. Si+Na (Fig. 9a), which show a rough positive correlation with a ratio close to 1:1. However, there is also distinctive discrepancy from the 1:1 line for higher Si+Na values (>0.03 apfu), which might imply that additional substitution mechanisms may have play a role such as (Pan and Fleet, 2002):

$$PO_4^{3-} + F^{-} \leftrightarrow SiO_4^{4-} + \square \quad (3)$$

$$Ca^{2+} + \square \leftrightarrow 2\ Na^{+} \quad (4)$$

In addition, the substitution of divalent cations (i.e. Fe^{2+}, Mn^{2+}, Sr^{2+}) for Ca^{2+} is also important:

$$Ca^{2+} \leftrightarrow (Fe, Mn, Sr)^{2+} \quad (5)$$

This substitution is illustrated in Fig. 9 (see also Supplementary Table 3, and compare Figs. 9a-b). The plot of Fe+Mn+Sr+Y+REEs vs. $X_{Cl\text{-}Ap}$ shown in Fig. 9b demonstrates that the amount of total substitutions of trivalent and divalent cations is positively related to X_{Ap}^{Cl}, suggesting that all these substitutions may have occurred leading to a general decrease of all trivalent and divalent cations (except Ca) with increasing metasomatic exchange.

In general, replacement reactions of apatite indicate changes in the properties of the coexisting liquid (melt or fluid) and/or in environmental conditions (i.e. temperature, pressure). In this study, for all three kinds of lithologies, secondary apatites have lower Cl and trace elements (Figs. 8-9), which is most probably the result of metasomatic reactions. Similar replacement textures and compositional variations of apatite have been widely observed in both fluid-dominated hydrothermal experiments (e.g. Yanagisawa et al., 1999; Harlov et al., 2002; Kusebauch et al., 2015) and in natural metasomatically overprinted rocks (e.g. Rae et al., 1996; Zirner et al., 2015). Kusebauch et al. (2015) noted that the X_{Ap}^{OH} of metasomatic apatite is more governed by OH^- concentration rather than Cl^- concentration in the fluid, indicating much higher incorporation tendency of OH than Cl for apatites in equilibrium with fluids at 200 MPa and 400-700 °C. Therefore, the increasing X_{Ap}^{OH} of the replaced zones of the apatites indicates that the fluid became more diluted with time, implying efficient cycling of hydrothermal fluids. The replaced apatites in the tonalites generally have higher X_{Ap}^{F} than those in the gabbros, plausibly due to dissolution of former magmatic high-F apatites in the hydrothermal fluids. Interestingly, the replaced apatites covering a wide X_{Ap}^{F} in the diorites range indicate a complex hydrothermal imprint (Fig. 10a), which may be due to the variability of the composition of the magmatic cores.

Metasomatism of apatites in a locally close system usually forms REE-rich minerals such as xenotime and monazite, either in the vicinity or even enclosed in the apatites (Harlov et al., 2002; Harlov, 2015; Zirner et al., 2015). However, such REE-rich minerals are absent in the investigated rocks (Figs. 4-6). We propose that the REEs were largely removed with dissolution of primary REE-rich apatites, and that the reprecipitation of secondary phases lead to strongly

REE-depleted apatites (Fig. 8), implying open-system conditions. Therefore, active penetration and circulation of seawater-derived fluids have strongly overprinted these intrusive rocks. This conclusion is consistent with the petrological evidence and cooling rate estimation on the metabasalts overlying a starving AML, which indicates very rapid cooling as a result of efficient circulation of hydrothermal fluids (Zhang et al., 2014).

Implications for petrogenesis of diorite: magma mixing

As described above, two types of magmatic apatite cores (Fig. 10a), i.e. high-Cl fluorapatite and low-F chlorapatite, have been observed in the intrusive rocks from IODP 1256D. Interestingly, although fluorapatite is absent in the gabbros and chlorapatite is absent in the tonalites, both types of apatite cores are present in the diorites. These contrasting compositions of the apatite cores of the diorites can be best explained by mixing/mingling of tonalitic and gabbroic magmas that already contained apatite as a crystalline phase (Fig. 10a). This model for the genesis of diorites is also consistent with the trace elemental characteristics of bulk rocks, which cannot be explained solely by fractional crystallization from gabbroic magmas but needs an input of tonalitic components (Zhang et al. submitted to Journal of Petrology). Therefore, in the following discussion, two kinds of melts are considered, one is the melt in equilibrium with fluorapatites (from tonalites) and the other is the melt in equilibrium with chlorapatite (from gabbros).

Magmatic apatites and implications for melt compositions

Exchange of F, Cl and OH between apatite and melt. The H_2O, F and Cl contents in a parental magma can be estimated using the composition of coexisting apatite if equilibrium is attained and if the partitioning behavior of these volatiles is well constrained. Numerous experiments on the distribution of F and Cl in apatite+melt±fluid systems have been performed in order to quantify their partitioning between apatite and melt (see review of Webster and Piccoli, 2015). In general, in terms of F, Cl and OH that are occupying the same site in the apatite structure, F is the most compatible, Cl is less compatible and but more than OH. However, strictly, the distribution behaviors of F, Cl and OH between apatite and melt (or fluid) are not best expressed as Henrian (or Nernst-type) partition coefficient (i.e., $D^{\mathrm{F}}_{\mathrm{Ap/melt}}$, $D^{\mathrm{Cl}}_{\mathrm{Ap/melt}}$ and

342 $D^{OH}_{Ap/melt}$), but rather should be treated as major elements (Boyce et al., 2014) in a comparable
343 way as that for Mg-Fe exchange between olivine and melt for example. It is emphasized that the
344 relative abundances of F, Cl and OH in apatite (i.e., X^{F}_{Ap}, X^{Cl}_{Ap} and X^{OH}_{Ap}) reflect the relative
345 activities of F, Cl and OH in the silicate melt or fluid that are in equilibrium with the apatite,
346 rather than absolute concentrations of these components in melt.

347 According to Boyce et al. (2014) and McCubbin et al. (2015), the exchange reaction between
348 apatite and melt in terms of F, Cl and OH can be described as:

349 $$A^{Ap} + B^{melt} \leftrightarrow B^{Ap} + A^{melt} \quad (6)$$

350 Here, A and B are F, Cl and OH. Assuming activity coefficients as unity, the equilibrium
351 exchange constant ($K^{A-B}_{Ap/melt}$) can be written as:

352 $$K^{A-B}_{Ap/melt} = (X^{A}_{Ap}/X^{B}_{Ap})/(X^{A}_{melt}/X^{B}_{melt}) \quad (7)$$

353 In this equation, X^{A}_{Ap} and X^{B}_{Ap} are endmember fractions in apatite (i.e., X^{F}_{Ap}, X^{Cl}_{Ap} or X^{OH}_{Ap}), and
354 X^{A}_{melt} are X^{B}_{melt} are molar fractions of the components A and B (i.e., F^-, Cl^- or OH^-) in melt.
355 Although the real activity coefficients may be complex functions depending on several factors
356 (e.g., temperature, pressure and system composition) and thus assumption of activity coefficients
357 as unity may not be valid, such treatment is more plausible than using Henrian partition
358 coefficients (Boyce et al., 2014). In fact, similar treatments have been applied to investigations
359 on the incorporations of F and Cl in apatite (Zhu and Sverjensky, 1992), biotite (Munoz, 1984)
360 and amphibole (Sato et al., 2005).

361 Mathez and Webster (2005) and Webster et al. (2009) performed experiments on the
362 partitioning behaviors of F and Cl between apatite and melt (±fluid) at 2 kbar for basaltic and
363 felsic systems respectively, and expressed the partitioning data as Henrian partition coefficients.
364 Boyce et al. (2014) reprocessed these experimental data in order to extract exchange coefficients.
365 However, the treatment of data in Boyce et al. (2014) and McCubbin et al. (2015) is based on the
366 assumption that total H_2O content in melt can be transferred as OH^-. As pointed out by Li and
367 Hermann (2015), such simplification might not be adequate considering our knowledge on the
368 existence of different water species in silicate melt following the dissociation reaction of water in

369 silicate melt (Stolper, 1982):

370 $H_2O_m + O^{2-} \leftrightarrow 2\ OH^-$ (8)

371 where H_2O_m is molecule water, O^{2-} is a bridging oxygen atom, and OH^- is a hydroxyl (not
372 bonded with H^+). Thus, the concentration of hydroxyl group is the specific component that
373 exchanges with OH in apatite (Eqs. 6-7).

374 Taking into account the issue of H_2O speciation in silicate melt, Li and Hermann (2015)
375 reprocessed the experimental data reported in Mathez and Webster (2005), Webster et al. (2009),
376 Doherty et al. (2014) and McCubbin et al. (2015), using the equilibrium constant K_{ws} of reaction
377 (8) determined for rhyolitic melt (Hui et al., 2008). It is emphasized that the melt compositions
378 for the apatite-related experiments (from rhyolitic to basaltic) and the melt composition (rhyolitic)
379 for the adopted K_{ws} are not identical, and thus potential errors are expected for the recalculated
380 exchange coefficients (K) given by Li and Hermann (2015). However, an assessment of such
381 potential errors is out the scope of this study. In this case, only the recalculated exchange
382 coefficients (K) by Li and Hermann (2015) based on the experiments of McCubbin et al. (2015)
383 were applied, because only in this study H_2O contents of melts were measured accurately by
384 SIMS, which provide highly reliable K values (see more detailed discussion in Li and Hermann,
385 2015). According to McCubbin et al. (2015) and Li and Hermann (2015), for systems with X_{Ap}^{F}
386 being 0.4-0.8, $K_{Ap/melt}^{F-OH}$ is determined as 50±7 (σ) and $K_{Ap/melt}^{Cl-OH}$ as 11±3 (σ). The consistent K
387 values over a wide range of X_{Ap}^{F} confirms the reliability of data and also implies that the
388 exchange coefficients do not vary within the investigated compositional range. However, for a F-
389 free system, McCubbin et al. (2015) found $K_{Ap/melt}^{Cl-OH}$ to be significantly higher with a value of
390 ~40. This large variation suggests that the exchange behavior of F-Cl-OH between apatite and
391 melt varies significantly for F-rich and F-poor systems. Therefore, in the following two sections,
392 we discuss the properties of melts assuming that they are in equilibrium with primary
393 fluorapatites (in tonalites and diorites) and with primary chlorapatites (in gabbros and diorites),
394 respectively. We believe that, despite a variety of uncertainties and approximations, our
395 quantitative estimation can still provide important constraints on the F and Cl abundances in the
396 intrusive magma bodies beneath fast-spreading MORs.

Melt in equilibrium with fluorapatite. Primary high-Cl fluorapatite cores exist in both tonalites and diorites, which show a small compositional field with $X_{\mathrm{Ap}}^{\mathrm{Cl}}$ within ca. 0.3-0.4 and with $X_{\mathrm{Ap}}^{\mathrm{F}}$ within ca. 0.4-0.6 (Fig. 7). Applying the *K* values according to McCubbin et al. (2015) and Li and Hermann (2015), the melts in equilibrium with the fluorapatites (from both tonalites and diorites) are estimated to have $X_{\mathrm{melt}}^{\mathrm{F}}/X_{\mathrm{melt}}^{\mathrm{OH}}$ of 0.09±0.04 (σ), $X_{\mathrm{melt}}^{\mathrm{Cl}}/X_{\mathrm{melt}}^{\mathrm{OH}}$ of 0.27±0.12 (σ) and $X_{\mathrm{melt}}^{\mathrm{F}}/X_{\mathrm{melt}}^{\mathrm{Cl}}$ of 0.28±0.03 (σ) (Fig. 10b). In the calculations, a few apatites in the diorites having $X_{\mathrm{Ap}}^{\mathrm{OH}}$ less than 0.05 are omitted in order to avoid extremely large $X_{\mathrm{melt}}^{\mathrm{F}}/X_{\mathrm{melt}}^{\mathrm{OH}}$ or $X_{\mathrm{melt}}^{\mathrm{Cl}}/X_{\mathrm{melt}}^{\mathrm{OH}}$ values that are unlikely.

The estimated $X_{\mathrm{melt}}^{\mathrm{F}}/X_{\mathrm{melt}}^{\mathrm{Cl}}$ ratio is independent on melt H_2O content, and thus its reliability is not associated with the uncertainty of estimation on melt H_2O content (see below). Wanless and Shaw (2012) measured the F and Cl concentrations of the melt inclusions and host glasses in the fresh lavas erupted at East Pacific Rise (EPR), which yield a molar F/Cl ratio of 5.2±2.1 (σ). Based on the apatite composition, the estimated molar F/Cl ratio of the melts for intrusive felsic magmas within the AML is ~0.3, which is significantly lower than that measured for the EPR lavas, supporting the idea that the felsic intrusive magmas cannot be evolved melts derived solely via fractional crystallization of MOR basaltic magmas, because both F and Cl are highly incompatible elements for all nominally-anhydrous minerals in basaltic systems (e.g. Beyer et al., 2012) and their ratio cannot vary significantly in melts. In addition, fractional crystallization of apatite can potentially decrease F/Cl ratio in evolved melts (e.g. Boyce et al., 2014), but this model is not supported by the fact that apatite is not observed or expected as an early phase in the fractional crystallization of MOR basaltic magmas (Zhang et al. submitted to Journal of Petrology). Furthermore, the magmatic apatite cores do not show evolving compositions in terms of F-Cl-OH, but exhibit nearly identical F/Cl ratios for gabbroic and tonalitic systems respectively.

Alternatively, partial melting of hydrothermally altered basaltic dikes (i.e., amphibole-bearing metabasalts) may be the origin of the felsic magmas at MORs (France et al., 2010; Wanless et al., 2010; Erdmann et al., 2015; Fischer et al., 2016). Hydrothermal amphibole is the major hydrous phase in the metabasalts in the dike-gabbro transition zone of fast-spreading MOR (Koepke et al., 2008; Alt et al., 2010), which is formed during the interval of periodical

426 magma replenishment of AML (Zhang et al., 2014). In this study, we measured amphibole
427 compositions for a typical hydrothermal vein collected from the dike-gabbro transition at IODP
428 Hole 1256D (335-U1256D-RUN19-RCJB-Rock C, ref. Teagle et al., 2012), and the contents of
429 F (0.21±0.03 wt%) and Cl (0.12±0.03 wt%) are both fairly homogeneous (see Supp. Table 4).
430 Because amphibole (or another hydrous phase) is absent in the melting residue, the molar F/Cl
431 ratio of the partial melt should be the same as that in the amphibole, i.e. 3.3±1.0 (σ) (Fig. 10b),
432 which is much higher than the estimated molar F/Cl ratio of melt (~0.3) based on the
433 fluorapatites. Therefore, another source with a low F/Cl ratio is necessary, and we propose that it
434 is most likely due to assimilation of seawater-derived high-chlorinity fluids (e.g. Michael and
435 Schilling, 1989; see discussions below).

436 In order to estimate the absolute concentrations of F and Cl in melt, the H_2O content should
437 be constrained independently. Experimental studies of France et al. (2010), Erdmann et al. (2015)
438 and Fischer et al. (2016) suggest that the tonalites beneath fast-spreading ridges can be
439 interpreted as partial melts of hydrous metabasalt, induced by heating of the underlying AML.
440 Importantly, the relatively low Al_2O_3 contents (ca. 11 wt%) of natural tonalites can only be
441 reproduced in experiments with very low water activity (most likely a_{H2O} <0.5), because more
442 plagioclase (the most Al-rich phase) is stabilized at low-a_{H2O} conditions (Erdmann et al., 2015).
443 In contrast, partial melts generated at water-saturated conditions usually have too high Al_2O_3
444 contents (ca. 15-18 wt%). Therefore, assuming a_{H2O} in the range of 0.1-0.3 at 0.5 kbar and a
445 plausible melting temperature of 950 °C (Erdmann et al., 2015; Fischer et al., 2016), the H_2O
446 content in tonalitic melts is estimated to be within 0.7-1.2 wt% (with application of the empirical
447 water solubility model of Moore et al., 1998). This value (1.0±0.2 wt% H_2O) was taken into
448 account for calculating F and Cl abundances in the melts from the estimated F-Cl-OH molar
449 ratios of melts based on the apatites, with application of the water species model of Hui et al.
450 (2008) [the same model was applied by Li and Hermann (2015) for calculating molar ratios of
451 F/OH and Cl/OH in silicate melts]. The calculated halogen concentrations of the tonalitic melts
452 in equilibrium with the fluorapatites are 0.04-0.16 wt% F and 0.12-0.48 wt% Cl.

453 The ranges of the F and Cl contents estimated above may represent the initial F and Cl
454 concentrations in the felsic melts at the beginning of the crystallization of apatite. Assuming that
455 common metabasalts contain 10-20 wt% amphibole with similar F and Cl contents as in the

456 hydrothermal amphiboles that we measured (0.21±0.03 wt% F and 0.12±0.03 wt% Cl; see also
457 Supp. Table 4), and that partial melting generates melts with a mass fraction of 20 wt% and the
458 residue contains no amphibole [which was confirmed by the experiments of Erdmann et al.
459 (2015)], we can estimate that the partial melts would contain 0.16±0.05 wt% F and 0.09±0.03 wt%
460 Cl. This melt F content is similar with the maximum F content estimated based on the
461 fluorapatites, suggesting that the F budget is coherent (F in melt estimated from source rock vs. F
462 in melt estimated from apatite). In contrast, the melt Cl content estimated from partial melting is
463 too low compared to the Cl contents estimated based on the fluorapatites, implying that an
464 additional high-Cl source has to be involved in the generation of the felsic melts. This source is
465 most probably seawater-derived high-chlorinity fluids (e.g. Michael and Schilling, 1989). Such
466 implications are consistent with the previous conclusions according to H_2O-independent F/Cl
467 ratios.

468 **Melt in equilibrium with chlorapatite**. Low-F chlorapatite cores exist in both gabbros and
469 diorites, which have a nearly identical composition with $X_{\mathrm{Ap}}^{\mathrm{Cl}}$ of 0.82 and $X_{\mathrm{Ap}}^{\mathrm{F}}$ of 0.03 (Fig. 7).
470 These high-Cl cores are interpreted as parts of the original magmatic apatites that crystallized in
471 the interstitial melts of gabbroic magmas. In the gabbros, their euhedral textures and
472 homogeneous compositions suggest that they might have crystallized from melts in which the
473 proportions of F/Cl/OH did not change significantly.

474 Cl-rich apatites with $X_{\mathrm{Ap}}^{\mathrm{Cl}}$ >0.8 have been commonly produced in melt-free apatite+fluid
475 systems (e.g. Fleet et al., 2000; Dong, 2005; Kusebauch et al., 2015; Hughes et al., 2016), but
476 rarely found in natural magmatic systems or experiments (Webster and Piccoli, 2015). However,
477 similar high-Cl apatites were synthesized by McCubbin et al. (2015) in a F-free apatite+melt
478 experiment with melt containing 1.37 wt% Cl, and a very high $K_{\mathrm{Ap/melt}}^{\mathrm{Cl-OH}}$ value of 41±9 (σ) (in
479 comparison with ~12 for other F-bearing systems) is derived from this experiment (Li and
480 Hermann, 2015). McCubbin et al. (2015) emphasized that the Cl-OH exchange behavior would
481 change substantially in F-bearing and F-free (or F-poor) systems. Although only one
482 experimental datum is existing for a F-free system, we can use it to estimate the Cl/OH ratio of
483 melts in equilibrium with the F-poor apatites ($X_{\mathrm{Ap}}^{\mathrm{F}}$ of ~0.03) from the gabbros and diorites.
484 However, it is emphasized that the calculated $X_{\mathrm{melt}}^{\mathrm{Cl}}/X_{\mathrm{melt}}^{\mathrm{OH}}$ value is a minimum value, because

increase of F would apparently decrease $K_{\mathrm{Ap/melt}}^{\mathrm{Cl-OH}}$ for low-F systems (McCubbin et al., 2015). Therefore, a minimum $X_{\mathrm{melt}}^{\mathrm{Cl}}/X_{\mathrm{melt}}^{\mathrm{OH}}$ value of ~0.14 for the melts in equilibrium with the chlorapatites is obtained, which is similar to the minimum $X_{\mathrm{melt}}^{\mathrm{Cl}}/X_{\mathrm{melt}}^{\mathrm{OH}}$ value estimated for tonalitic melts in equilibrium with the fluorapatites (ranging in 0.27±0.12, see above). More accurate estimation on the Cl concentrations is difficult due to the lack of a large experimental database for F-poor systems, but it is clear that the F/Cl ratio and the Cl content in the melts in equilibrium with the chlorapatites must be higher than that in the melts in equilibrium with the fluorapatites (Fig. 10b). Therefore, fractional crystallization of MOR basaltic melts plus assimilation of the felsic melts cannot fully explain the highly elevated Cl in gabbroic magmas to form the extremely Cl-rich apatites ($X_{\mathrm{Ap}}^{\mathrm{Cl}}$ ~0.82), and another high-Cl component (e.g. seawater-derived brine) may also be involved (see discussions below).

Implications for brine assimilation by magmas in AML

The discussions above indicate that the melts in equilibrium with the apatites should have assimilated high-Cl components in order to form the magmatic cores of high-Cl fluorapatite (in tonalites) and low-F chlorapatites (in gabbros). To explain the abnormally high Cl concentrations in some MOR basaltic lavas at fast-spreading ridges, the low Cl/F and Cl/H_2O ratios of the hydrothermal amphibole-bearing metabasalts in the dike-gabbro transition zone, as well as felsic melts that may be derived by partial melting of the metabasalts, can be excluded as dominant assimilants (Michael and Schilling, 1989; Fischer et al., 2016; this study, Supp. Table 4). Alternatively, assimilation of seawater-derived Cl-rich brines, which can have very high Cl/F and Cl/H_2O ratios, by magmas at the boundary of AML, may be a plausible process (e.g. Bischoff and Rosenbauer, 1989; Michael and Schilling, 1989; Kendrick et al., 2013). Such high-salinity fluids (up to 50 wt% equivalent NaCl) have been documented as fluid inclusions in hydrothermally altered oceanic crusts (Kelley and Delaney, 1987; Nehlig, 1991). In addition, Meurer and Natland (2001) documented apatites with $X_{\mathrm{Ap}}^{\mathrm{Cl}}$ up to 0.85 in the cumulate gabbros from Hess Deep, and the high-Cl characteristics were similarly interpreted by the authors to be due to assimilation of high-Cl seawater-derived fluids.

Fig. 10c shows the isobaric phase projection of the NaCl-H_2O system at 0.5 kbar (Driesner and Heinrich, 2007), which explains the formation of high-salinity fluids from a low-salinity

514 fluid. If a seawater-like initial fluid (point A) is transported to a depth above the AML, being
515 heated up by the underlying AML magmas, a high salinity brine and a low salinity vapor can
516 form as a result of phase separation (i.e. hydrothermal boiling). The NaCl content of the brine
517 increases with increasing temperature, but its relative mass to the vapor phase decreases as
518 controlled by mass balance. For example, assuming a high temperature of 900 °C, the salinity of
519 the brine could be 90 wt% NaCl (point B). Because petrological evidence indicates that the
520 recrystallization temperature of metabasalts overlying the AML could be up to 1050 °C (Koepke
521 et al., 2008; France et al., 2009; Alt et al., 2010; Zhang et al., 2014), and because partial melting
522 of metabasalt occurs at temperatures >900 °C (Erdmann et al., 2015; Fischer et al., 2016), the
523 fluid evolution towards high salinity brines can be achieved in the absence of melt until
524 temperatures above 900 °C. At higher temperatures when melt starts to be present, the high-
525 density brine phase would be an ideal assimilant for enriching Cl in the magmatic system. In this
526 scenario, the low-density vapor phase would escape rapidly to shallower depths (Bischoff and
527 Rosenbauer, 1989; Alt et al., 2010).

528 Continuous cycling of seawater-derived fluids overlying the AML (Sleep, 1991; Phipps
529 Morgan and Chen, 1993) implies that an open system of Cl needs to be assumed for magmatic
530 and hydrothermal processes at MORs. Assimilation of the high-Cl brines in the felsic and
531 gabbroic magmas will strongly increase Cl concentration and Cl/F ratio in the melts, which can
532 easily explain the high-Cl magmatic apatite cores (Fig. 10b). It is difficult to determine the exact
533 salinity of the brines assimilated by the silicate melts and the brine/melt ratio during assimilation,
534 but we propose that the salinity of assimilated fluid must be very high and the fluid/melt ratio
535 must be very low, because: (1) of the high-Cl features of the melts in equilibrium with the
536 magmatic apatites (Fig. 10b), (2) of the properties of the fluids as a result of hydrothermal
537 boiling at high temperatures (Fig. 10c), and (3) of the low H_2O activities prevailing in the
538 magmatic systems (for example, magmatic amphibole is absent in the felsic intrusives and very
539 rare in the gabbroic intrusives). Therefore, the hypothesis that MOR magmatic systems at fast-
540 spreading ridges have been assimilated by high-Cl brines, which was previously invoked to
541 interpret the over-enrichment of Cl in erupted MOR lavas (e.g. Michael and Schilling, 1989;
542 Kendrick et al., 2013), is also supported by the magmatic apatites from an intact MOR intrusive
543 crust.

ACKNOWLEDGEMENTS

We gratefully acknowledge the shipboard crew and Scientific Party of IODP Expeditions 312 and 335 for their assistance in data collection. The samples used in this study were provided by the Integrated Ocean Drilling Program. We thank Michael A.W. Marks (University of Tübingen) for sharing the reference Durango apatite. The manuscript was benefited significantly from comments of Jim Webster, Romain Tartese and other three anonymous reviewers. This research was funded by the DFG (German Research Foundation) project KO 1723/17.

REFERENCES CITED

Alt, J.C. (1995) Subseafloor Processes in Mid-Ocean Ridge Hydrothennal Systems. Seafloor Hydrothermal Systems: Physical, Chemical, Biological, and Geological Interactions, p. 85-114. American Geophysical Union.

Alt, J.C., Laverne, C., Coggon, R.M., Teagle, D.A.H., Banerjee, N.R., Morgan, S., Smith-Duque, C.E., Harris, M., and Galli, L. (2010) Subsurface structure of a submarine hydrothermal system in ocean crust formed at the East Pacific Rise, ODP/IODP Site 1256. Geochemistry Geophysics Geosystems, 11(10), Q10010.

Beyer, C., Klemme, S., Wiedenbeck, M., Stracke, A., and Vollmer, C. (2012) Fluorine in nominally fluorine-free mantle minerals: Experimental partitioning of F between olivine, orthopyroxene and silicate melts with implications for magmatic processes. Earth and Planetary Science Letters, 337–338(0), 1-9.

Bischoff, J.L., and Rosenbauer, R.J. (1989) Salinity variations in submarine hydrothermal systems by layered double-diffusive convection. Journal of Geology, 97(5), 613-623.

Boudreau, A.E., and McCallum, I.S. (1990) Low temperature alteration of REE-rich chlorapatite from the Stillwater Complex, Montana. American Mineralogist, 75(5-6), 687-693.

Boyce, J.W., Tomlinson, S.M., McCubbin, F.M., Greenwood, J.P., and Treiman, A.H. (2014) The Lunar Apatite Paradox. Science, 344(6182), 400-402.

Brenan, J. (1994) Kinetics of fluorine, chlorine and hydroxyl exchange in fluorapatite. Chemical Geology, 110(1-3), 195-210.

Cherniak, D.J. (2000) Rare earth element diffusion in apatite. Geochimica et Cosmochimica Acta, 64(22), 3871-3885.

Colman, A., Sinton, J.M., White, S.M., McClinton, J.T., Bowles, J.A., Rubin, K.H., Behn, M.D., Cushman, B., Eason, D.E., and Gregg, T.K. (2012) Effects of variable magma supply on mid-ocean ridge eruptions: Constraints from mapped lava flow fields along the Galápagos Spreading Center. Geochemistry Geophysics Geosystems, 13(8), Q08014.

Coogan, L.A. (2014) The Lower Oceanic Crust. In H.D. Holland, and K.K. Turekian, Eds. Treatise on Geochemistry (Second Edition), p. 497-541. Elsevier, Oxford.

Coogan, L.A., Mitchell, N.C., and O'Hara, M.J. (2003) Roof assimilation at fast spreading ridges: An investigation combining geophysical, geochemical, and field evidence. Journal of Geophysical Research, 108(B1), 2002.

Coogan, L.A., Wilson, R.N., Gillis, K.M., and MacLeod, C.J. (2001) Near-solidus evolution of oceanic gabbros: insights from amphibole geochemistry. Geochimica et Cosmochimica Acta, 65(23), 4339-4357.

585 Doherty, A.L., Webster, J.D., Goldoff, B.A., and Piccoli, P.M. (2014) Partitioning behavior of chlorine
586 and fluorine in felsic melt–fluid(s)–apatite systems at 50 MPa and 850–950 °C. Chemical
587 Geology, 384, 94-111.
588 Dong, P. (2005) Halogen-element (F, Cl, and Br) behaviour in apatites, scapolite, and sodalite: an
589 experimental investigation with field applications, Ph.D., p. 234. University of Saskatchewan,
590 Saskatoon.
591 Driesner, T., and Heinrich, C.A. (2007) The system H_2O–NaCl. Part I: Correlation formulae for phase
592 relations in temperature–pressure–composition space from 0 to 1000 °C, 0 to 5000 bar, and 0 to 1
593 X_{NaCl}. Geochimica et Cosmochimica Acta, 71(20), 4880-4901.
594 Erdmann, M., Fischer, L., France, L., Zhang, C., Godard, M., and Koepke, J. (2015) Anatexis at the roof
595 of an oceanic magma chamber at IODP Site 1256 (equatorial Pacific): an experimental study.
596 Contributions to Mineralogy and Petrology, 169(4), 1-28.
597 Fischer, L.A., Erdmann, M., France, L., Wolff, P.E., Deloule, E., Zhang, C., Godard, M., and Koepke, J.
598 (2016) Trace element evidence for anatexis at oceanic magma chamber roofs and the role of
599 partial melts for contamination of fresh MORB. Lithos, 260, 1-8.
600 Fleet, M.E., Liu, X., and Pan, Y. (2000) Rare-earth elements in chlorapatite [Ca10(PO4)6Cl2]: Uptake,
601 site preference, and degradation of monoclinic structure. American Mineralogist, 85, p. 1437-
602 1446.
603 Fontaine, F.J., Wilcock, W.S.D., and Butterfield, D.A. (2007) Physical controls on the salinity of mid-
604 ocean ridge hydrothermal vent fluids. Earth and Planetary Science Letters, 257(1–2), 132-145.
605 France, L., Ildefonse, B., and Koepke, J. (2009) Interactions between magma and hydrothermal system in
606 Oman ophiolite and in IODP Hole 1256D: Fossilization of a dynamic melt lens at fast spreading
607 ridges. Geochemistry Geophysics Geosystems, 10(10), Q10O19.
608 France, L., Koepke, J., Ildefonse, B., Cichy, S., and Deschamps, F. (2010) Hydrous partial melting in the
609 sheeted dike complex at fast spreading ridges: experimental and natural observations.
610 Contributions to Mineralogy and Petrology, 160(5), 683-704.
611 France, L., Koepke, J., MacLeod, C.J., Ildefonse, B., Godard, M., and Deloule, E. (2014) Contamination
612 of MORB by anatexis of magma chamber roof rocks: Constraints from a geochemical study of
613 experimental melts and associated residues. Lithos, 202-203, 120-137.
614 Freund, S., Beier, C., Krumm, S., and Haase, K.M. (2013) Oxygen isotope evidence for the formation of
615 andesitic–dacitic magmas from the fast-spreading Pacific–Antarctic Rise by assimilation–
616 fractional crystallisation. Chemical Geology, 347(0), 271-283.
617 Gillis, K.M. (2008) The roof of an axial magma chamber: A hornfelsic heat exchanger. Geology, 36(4),
618 299-302.
619 Gillis, K.M., Coogan, L.A., and Chaussidon, M. (2003) Volatile element (B, Cl, F) behaviour in the roof
620 of an axial magma chamber from the East Pacific Rise. Earth and Planetary Science Letters,
621 213(3–4), 447-462.
622 Goldoff, B., Webster, J.D., and Harlov, D.E. (2012) Characterization of fluor-chlorapatites by electron
623 probe microanalysis with a focus on time-dependent intensity variation of halogens. American
624 Mineralogist, 97(7), 1103-1115.
625 Guillong, M., Meier, D., Allan, M., Heinrich, C., and Yardley, B. (2008) SILLS: a MATLAB-based
626 program for the reduction of laser ablation ICP-MS data of homogeneous materials and
627 inclusions. Mineralogical Association of Canada Short Course, 40, 328-333.
628 Harlov, D.E. (2015) Apatite: A Fingerprint for Metasomatic Processes. Elements, 11(3), 171-176.
629 Harlov, D.E., Förster, H.-J., and Nijland, T.G. (2002) Fluid-induced nucleation of (Y+ REE)-phosphate
630 minerals within apatite: nature and experiment. Part I. Chlorapatite. American Mineralogist, 87(2-
631 3), 245-261.
632 Harlov, D.E., Wirth, R., and Förster, H.-J. (2005) An experimental study of dissolution–reprecipitation in
633 fluorapatite: fluid infiltration and the formation of monazite. Contributions to Mineralogy and
634 Petrology, 150(3), 268-286.

Harris, M., Coggon, R.M., Smith-Duque, C.E., Cooper, M.J., Milton, J.A., and Teagle, D.A.H. (2015) Channelling of hydrothermal fluids during the accretion and evolution of the upper oceanic crust: Sr isotope evidence from ODP Hole 1256D. Earth and Planetary Science Letters, 416(0), 56-66.

Horn, I., von Blanckenburg, F., Schoenberg, R., Steinhoefel, G., and Markl, G. (2006) In situ iron isotope ratio determination using UV-femtosecond laser ablation with application to hydrothermal ore formation processes. Geochimica et Cosmochimica Acta, 70(14), 3677-3688.

Hughes, J.M. (2015) The many facets of apatite. American Mineralogist, 100(5-6), 1033-1039.

Hughes, J.M., Harlov, D.E., Kelly, S.R., Rakovan, J., and Wilke, M. (2016) Solid solution in the apatite OH-Cl binary system: compositional dependence of solid solution mechanisms in calcium phosphate apatites along the Cl-OH binary. American Mineralogist, 101, 1783-1791.

Hui, H., Zhang, Y., Xu, Z., and Behrens, H. (2008) Pressure dependence of the speciation of dissolved water in rhyolitic melts. Geochimica et Cosmochimica Acta, 72(13), 3229-3240.

Kelley, D.S., and Delaney, J.R. (1987) Two-phase separation and fracturing in mid-ocean ridge gabbros at temperatures greater than 700 C. Earth and Planetary Science Letters, 83(1), 53-66.

Kendrick, M.A., Arculus, R., Burnard, P., and Honda, M. (2013) Quantifying brine assimilation by submarine magmas: Examples from the Galápagos Spreading Centre and Lau Basin. Geochimica et Cosmochimica Acta, 123(0), 150-165.

Kent, G.M., Harding, A.J., and Orcutt, J.A. (1990) Evidence for a smaller magma chamber beneath the East Pacific Rise at 9°30' N. Nature, 344(6267), 650-653.

Koepke, J., Christie, D.M., Dziony, W., Holtz, F., Lattard, D., Maclennan, J., Park, S., Scheibner, B., Yamasaki, T., and Yamazaki, S. (2008) Petrography of the dike-gabbro transition at IODP Site 1256 (equatorial Pacific): The evolution of the granoblastic dikes. Geochemistry Geophysics Geosystems, 9(7), Q07O09.

Koepke, J., France, L., Müller, T., Faure, F., Goetze, N., Dziony, W., and Ildefonse, B. (2011) Gabbros from IODP Site 1256, equatorial Pacific: Insight into axial magma chamber processes at fast spreading ocean ridges. Geochemistry Geophysics Geosystems, 12(9), Q09014.

Kusebauch, C., John, T., Whitehouse, M.J., Klemme, S., and Putnis, A. (2015) Distribution of halogens between fluid and apatite during fluid-mediated replacement processes. Geochimica et Cosmochimica Acta, 170, 225-246.

Li, H., and Hermann, J. (2015) Apatite as an indicator of fluid salinity: An experimental study of chlorine and fluorine partitioning in subducted sediments. Geochimica et Cosmochimica Acta, 166, 267-297.

Maclennan, J., Hulme, T., and Singh, S.C. (2005) Cooling of the lower oceanic crust. Geology, 33(5), 357-366.

Marks, M.A.W., Wenzel, T., Whitehouse, M.J., Loose, M., Zack, T., Barth, M., Worgard, L., Krasz, V., Eby, G.N., Stosnach, H., and Markl, G. (2012) The volatile inventory (F, Cl, Br, S, C) of magmatic apatite: An integrated analytical approach. Chemical Geology, 291, 241-255.

Mathez, E.A., and Webster, J.D. (2005) Partitioning behavior of chlorine and fluorine in the system apatite-silicate melt-fluid. Geochimica et Cosmochimica Acta, 69(5), 1275-1286.

McCubbin, F.M., Vander Kaaden, K.E., Tartèse, R., Boyce, J.W., Mikhail, S., Whitson, E.S., Bell, A.S., Anand, M., Franchi, I.A., Wang, J., and Hauri, E.H. (2015) Experimental investigation of F, Cl, and OH partitioning between apatite and Fe-rich basaltic melt at 1.0–1.2 GPa and 950–1000 °C. American Mineralogist, 100(8-9), 1790-1802.

Meurer, W.P., and Natland, J.H. (2001) Apatite compositions from oceanic cumulates with implications for the evolution of mid-ocean ridge magmatic systems. Journal of Volcanology and Geothermal Research, 110(3–4), 281-298.

Michael, P.J., and Schilling, J.-G. (1989) Chlorine in mid-ocean ridge magmas: Evidence for assimilation of seawater-influenced components. Geochimica et Cosmochimica Acta, 53(12), 3131-3143.

Moore, G., Vennemann, T., and Carmichael, I.S.E. (1998) An empirical model for the solubility of H_2O in magmas to 3 kilobars. American Mineralogist, 83(1-2), 36-42.

685 Munoz, J.L. (1984) F-OH and Cl-OH exchange in micas with applications to hydrothermal ore deposits.
686 Reviews in Mineralogy, 13(1), 469-493.
687 Nehlig, P. (1991) Salinity of oceanic hydrothermal fluids: a fluid inclusion study. Earth and Planetary
688 Science Letters, 102(3–4), 310-325.
689 Nehlig, P. (1993) Interactions between magma chambers and hydrothermal systems: Oceanic and
690 ophiolitic constraints. Journal of Geophysical Research, 98(B11), 19621-19633.
691 Pan, Y., and Fleet, M.E. (2002) Compositions of the Apatite-Group Minerals: Substitution Mechanisms
692 and Controlling Factors. Reviews in Mineralogy and Geochemistry, 48(1), 13-49.
693 Pearce, N.J., Perkins, W.T., Westgate, J.A., Gorton, M.P., Jackson, S.E., Neal, C.R., and Chenery, S.P.
694 (1997) A compilation of new and published major and trace element data for NIST SRM 610 and
695 NIST SRM 612 glass reference materials. Geostandards Newsletter, 21(1), 115-144.
696 Phipps Morgan, J., and Chen, Y.J. (1993) The Genesis of Oceanic Crust: Magma Injection, Hydrothermal
697 Circulation, and Crustal Flow. Journal of Geophysical Research, 98(B4), 6283-6297.
698 Piccoli, P.M., and Candela, P.A. (2002) Apatite in Igneous Systems. Reviews in Mineralogy and
699 Geochemistry, 48(1), 255-292.
700 Putnis, A., and John, T. (2010) Replacement Processes in the Earth's Crust. Elements, 6(3), 159-164.
701 Rae, D.A., Coulson, I.M., and Chambers, A.D. (1996) Metasomatism in the North Qôroq centre, South
702 Greenland: apatite chemistry and rare-earth element transport. Mineralogical Magazine, 60(398),
703 207-220.
704 Rannou, E., Caroff, M., and Cordier, C. (2006) A geochemical approach to model periodically
705 replenished magma chambers: Does oscillatory supply account for the magmatic evolution of
706 EPR 17–19°S? Geochimica et Cosmochimica Acta, 70(18), 4783-4796.
707 Sato, H., Holtz, F., Behrens, H., Botcharnikov, R., and Nakada, S. (2005) Experimental Petrology of the
708 1991–1995 Unzen Dacite, Japan. Part II: Cl/OH Partitioning between Hornblende and Melt and
709 its Implications for the Origin of Oscillatory Zoning of Hornblende Phenocrysts. Journal of
710 Petrology, 46(2), 339-354.
711 Sleep, N.H. (1991) Hydrothermal circulation, anhydrite precipitation, and thermal structure at ridge axes.
712 Journal of Geophysical Research, 96(B2), 2375-2387.
713 Stolper, E. (1982) Water in silicate glasses: An infrared spectroscopic study. Contributions to Mineralogy
714 and Petrology, 81(1), 1-17.
715 Stormer, J.C., Pierson, M.L., and Tacker, R.C. (1993) Variation of F and Cl X-ray intensity due to
716 anisotropic diffusion in apatite during electron microprobe analysis. American Mineralogist, 78,
717 641-648.
718 Sun, S.S., and McDonough, W.F. (1989) Chemical and isotopic systematics of oceanic basalts:
719 implications for mantle compositions and processes. In A.D. Saunders, and M.J. Norry, Eds.
720 Magmatism in the Ocean Basins, 42, p. 313-345. Geological Society of London.
721 Tacker, R.C., and Stormer, J.C. (1989) A thermodynamic model for apatite solid solutions, applicable to
722 high-temperature geologic problems. American Mineralogist, 74(7-8), 877-888.
723 Teagle, D.A.H., Alt, J.C., Umino, S., S. Miyashita, Banerjee, N.R., Wilson, D.S., and the Expedition
724 309/312 Scientists. (2006) Proceedings of the Integrated Ocean Drilling Program, vol. 309/312.
725 Ocean Drill. Program.
726 Teagle, D.A.H., Ildefonse, B., Blum, P., and Scientists, t.E. (2012) Proceedings of the Integrated Ocean
727 Drilling Program, vol. 335. Integrated Ocean Drilling Program Management International, Inc.,
728 Tokyo.
729 Wang, L.-X., Marks, M.A.W., Wenzel, T., Von Der Handt, A., Keller, J., Teiber, H., and Markl, G. (2014)
730 Apatites from the Kaiserstuhl Volcanic Complex, Germany: new constraints on the relationship
731 between carbonatite and associated silicate rocks. European Journal of Mineralogy, 26, 397-414.
732 Wanless, V.D., Perfit, M.R., Ridley, W.I., and Klein, E. (2010) Dacite Petrogenesis on Mid-Ocean Ridges:
733 Evidence for Oceanic Crustal Melting and Assimilation. Journal of Petrology, 51(12), 2377-2410.
734 Wanless, V.D., and Shaw, A.M. (2012) Lower crustal crystallization and melt evolution at mid-ocean
735 ridges. Nature Geoscience, 5(9), 651-655.

Webster, J.D., and Piccoli, P.M. (2015) Magmatic Apatite: A Powerful, Yet Deceptive, Mineral. Elements, 11(3), 177-182.

Webster, J.D., Tappen, C.M., and Mandeville, C.W. (2009) Partitioning behavior of chlorine and fluorine in the system apatite–melt–fluid. II: Felsic silicate systems at 200 MPa. Geochimica et Cosmochimica Acta, 73(3), 559-581.

Wilson, D.S., Teagle, D.A.H., and et al. (2006) Drilling to Gabbro in Intact Ocean Crust. Science, 312(5776), 1016-1020.

Yanagisawa, K., Rendon-Angeles, J.C., Ishizawa, N., and Oishi, S. (1999) Topotaxial replacement of chlorapatite by hydroxyapatite during hydrothermal ion exchange. American Mineralogist, 84(11-12), 1861-1869.

Young, E.J., Myers, A.T., Munson, E.L., and Conklin, N.M. (1969) Mineralogy and geochemistry of fluorapatite from Cerro de Mercado, Durango, Mexico. U.S. Geological Survey of Professional Paper 650-D, D84-D93.

Zhang, C., Holtz, F., Ma, C., Wolff, P., and Li, X. (2012) Tracing the evolution and distribution of F and Cl in plutonic systems from volatile-bearing minerals: a case study from the Liujiawa pluton (Dabie orogen, China). Contributions to Mineralogy and Petrology, 164, 859-879.

Zhang, C., Koepke, J., Kirchner, C., Götze, N., and Behrens, H. (2014) Rapid hydrothermal cooling above the axial melt lens at fast-spreading mid-ocean ridge. Scientific Reports, 4, No. 6342. DOI: 10.1038/srep06342.

Zhang, C., Koepke, J., Wang, L.-X., Wolff, P.E., Wilke, S., Stechern, A., Almeev, R., and Holtz, F. (2015) A Practical Method for Accurate Measurement of Trace Level Fluorine in Mg- and Fe-Bearing Mineral and Glass Using Electron Probe Microanalysis. Geostandards and Geoanalytical Research, DOI: 10.1111/j.1751-908X.2015.00390.x.

Zhu, C., and Sverjensky, D.A. (1992) F-Cl-OH partitioning between biotite and apatite. Geochimica et Cosmochimica Acta, 56(9), 3435-3467.

Zirner, A.L.K., Marks, M.A.W., Wenzel, T., Jacob, D.E., and Markl, G. (2015) Rare earth elements in apatite as a monitor of magmatic and metasomatic processes: The Ilímaussaq complex, South Greenland. Lithos, 228–229(0), 12-22.

776 **Figure 1.** Map of eastern Pacific Ocean showing the location of IODP Hole 1256D. Also shown is the
777 age pattern of seafloors around the mid-ocean ridge of East Pacific Rise, which indicates that the oceanic
778 crust at Hole 1256D was formed by superfast spreading with a full spreading rate of ca. 210 mm/year
779 (after Wilson et al. 2006).

780

781 **Figure 2.** MgO versus FeO_T for all lithologies recovered from IODP Hole 1256D. FeO_T is total iron
782 expressed as FeO. Data are compiled from Yamazaki et al. (2009), Neo et al. (2009), Sano et al. (2011),
783 Expedition 335 Scientists (2012) and Zhang et al. (submitted to Journal of Petrology).

784

785 **Figure 3.** Petrography of felsic to gabbroic intrusive rocks. (a) Scan of thin section of sample 214-2-P10,
786 showing dioritic patch within gabbro. The gabbro domains, outlined by dashed curves, are characterized
787 by subophitic texture and composed of poikilitic clinopyroxene and enclosed skeletal plagioclase. The
788 dioritic patch domain is interconnected, composed of amphibole, Fe-Ti oxides, plagioclase, albite, quartz
789 and apatite. The transition between these two domains are gradual, usually showing amphibole replacing
790 former clinopyroxene. (b) Scan of thin section of sample 235-1-P5. The dashed curves indicate the
791 uneven intrusive boundaries between the tonalitic vein and diorite wall-rock.

792

793 **Figure 4.** BSE images and X-ray maps of apatites in tonalites. (a) Sample 214-1-P14. (b) Sample 235-1-
794 P5. White curves outline the boundaries of apatites. Note that two apatite crystals contact each other in (b).
795 Note that the brightness of F Kα mapping on magnetite or chlorite is resulted from spectral interference of
796 Fe on F Kα. However, brightness of F Kα mapping on apatite does reflect their relative F abundances,
797 because the trace Fe in apatite has little interference on F Kα (see Zhang et al., 2015). Mineral
798 abbreviations: Act, actinolite; Ab, albite; Ap, apatite; Chl, chlorite; Ilm, ilmenite; Mgt, magnetite; Plg,
799 plagioclase; Py, pyrite; Qtz, quartz; Tnt, titanite.

800

801 **Figure 5.** BSE images and X-ray maps of apatites in diorites. (a) Sample 214-1-P10. (b) Sample 214-2-
802 P10. White curves outline the boundaries of apatites. Horizontal arrows indicates emplaced zones formed
803 prior to those indicated by vertical arrows. See notes and mineral abbreviations in Fig. 4.

804

805 **Figure 6.** BSE images and X-ray maps of apatites in gabbros. (a) Sample 232-2-P1. (b) Sample 216-1-
806 P13. White curves outline the boundaries of apatites. Horizontal arrows indicates emplaced zones formed
807 prior to those indicated by vertical arrows. See notes and mineral abbreviations in Fig. 4.

808

809 **Figure 7.** Apatite compositional variation of F, Cl and OH. (a) Binary plot of Cl vs. F contents. (b)
810 Triangular plot of molar proportion of OH-Ap, F-Ap and Cl-Ap endmembers. Grey solid lines in (b)
811 indicate the boundaries of endmembers.

Figure 8. Apatite compositional variation of REEs. (a) Apatite in tonalite. (b) Apatite in diorite. (c) Apatite in gabbro. Note the general depletion in REEs of rim compared to core.

Figure 9. Substitution of cations in apatite. (a) Y+REEs vs. Si+Na. The solid line in (a) is 1:1 line. (b) Fe+Mn+Sr+Y+REEs vs. $X_{\mathrm{Ap}}^{\mathrm{Cl}}$.

Figure 10. Compositional variations of apatite, melt and fluid. (a) Triangular plot of OH-Ap, F-Ap and Cl-Ap. (b) Triangular plot of molar fractions of OH, F and Cl in silicate melts (see text for estimation). Crustal partial melt corresponds to the felsic melt derived from amphibole-bearing metabasalt and is estimated based on hydrothermal amphibole compositions. EPR basaltic glass corresponds to the average composition of melt inclusions and host glasses in the fresh lavas erupted at East Pacific Rise (Wanless and Shaw, 2012). Type-1 melt corresponds to the melt in equilibrium with the fluorapatites. Type-2 melt corresponds to the estimated melt composition in equilibrium with the chlorapatites (the question mark denotes that its composition is not quantified but only estimated based on higher Cl/OH and low F/OH ratio of the chlorapatites compared to the fluorapatites). The composition of brine (full range on the inset diagram) corresponds to a range of chlorinity of 50-90 wt% equivalent NaCl. (c) Isobaric projection of the coexisting phases (i.e. vapor and brine) in the system NaCl-H_2O at 0.5 kbar (calculated using the program SoWat, Driesner and Heinrich 2007).

Figure 1

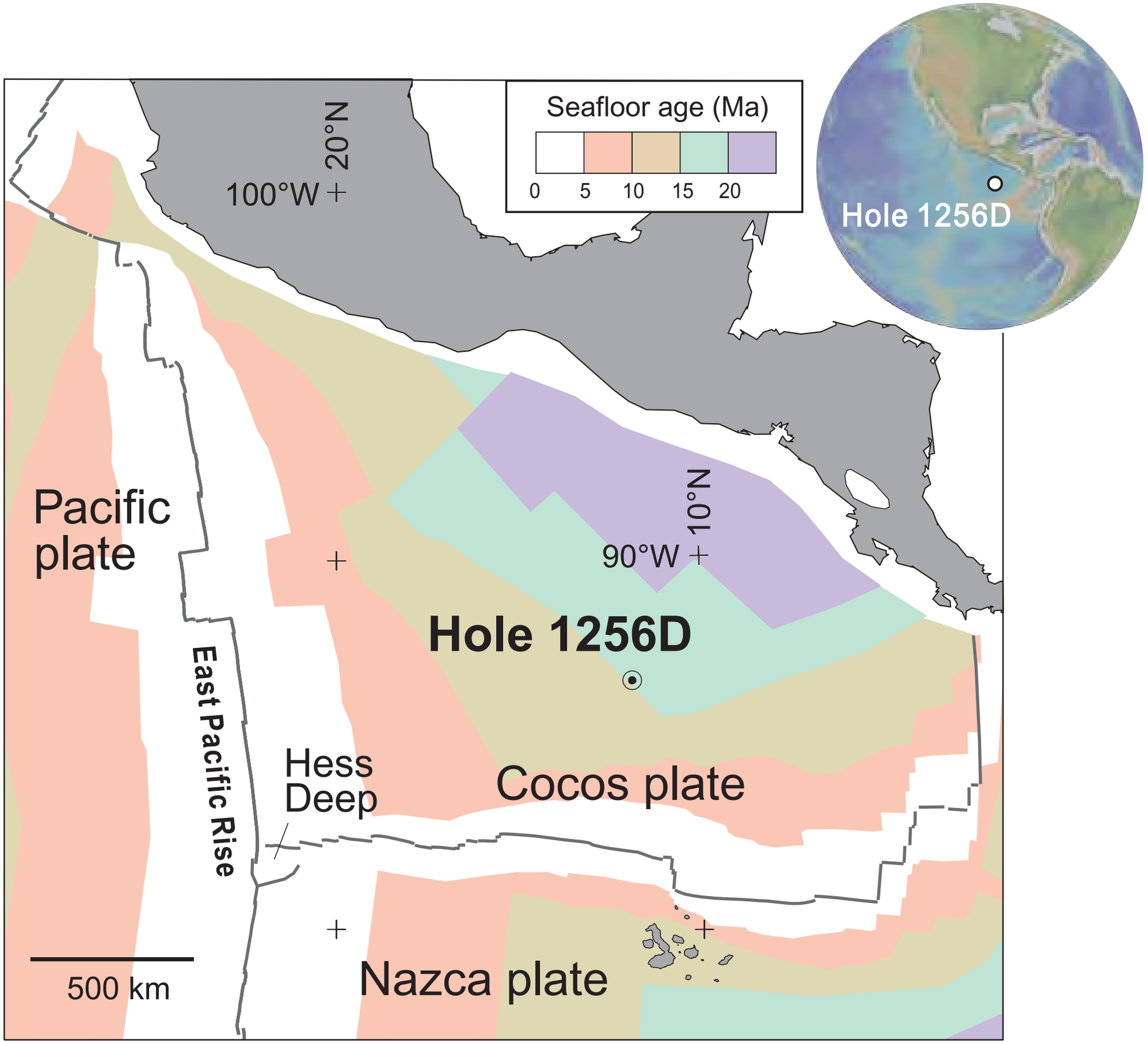
Seafloor age (Ma)
0
5
10
15
20
Hole 1256D
20°N
100°W
10°N
90°W
Pacific plate
East Pacific Rise
Hess Deep
Cocos plate
Nazca plate
500 km

Figure 2

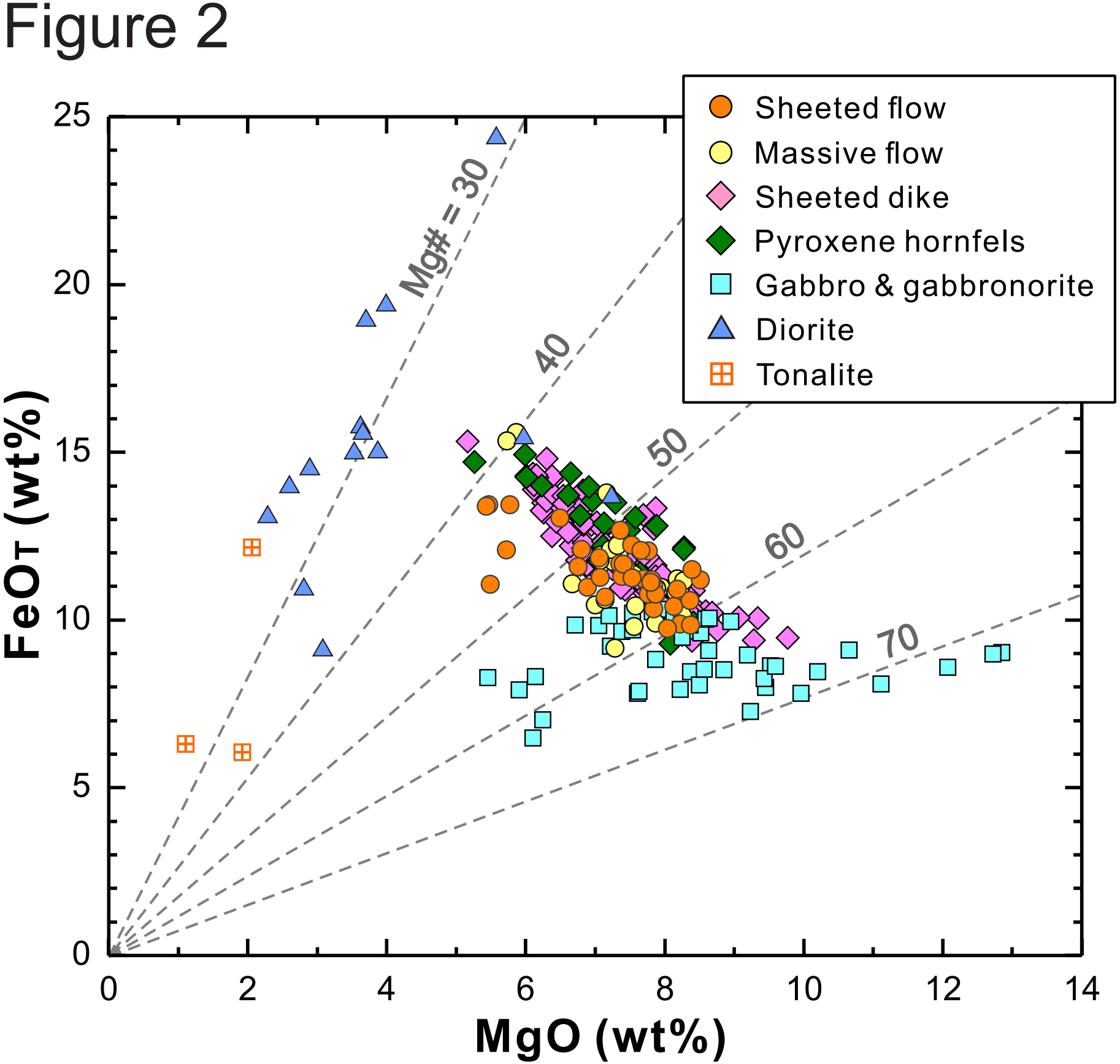
Sheeted flow
Massive flow
Sheeted dike
Pyroxene hornfels
Gabbro & gabbronorite
Diorite
Tonalite
Mg# = 30
40
50
60
70
FeOT (wt%)
MgO (wt%)
0
5
10
15
20
25
0
2
4
6
8
10
12
14

Figure 3

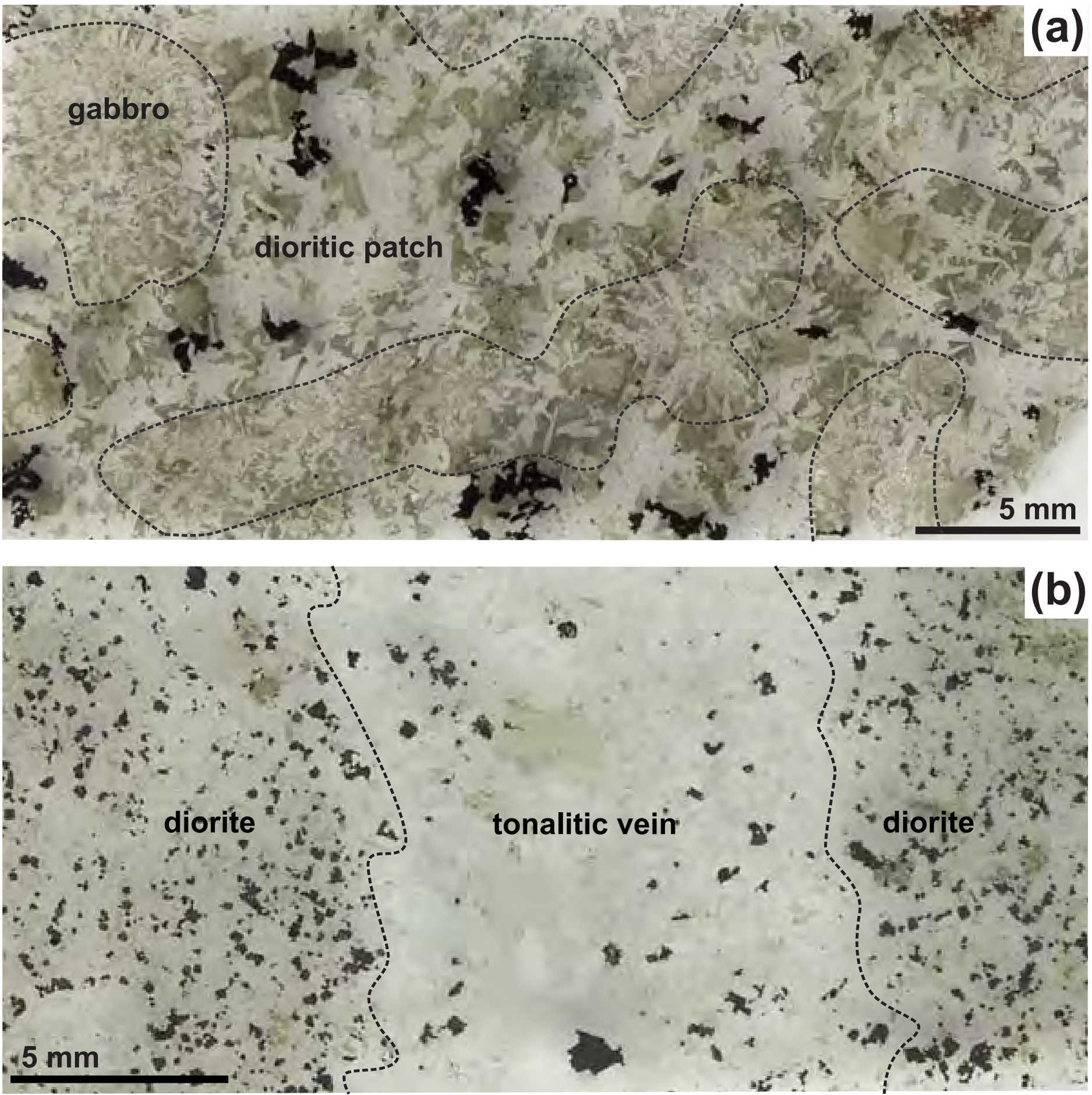
(a)
gabbro
dioritic patch
5 mm
(b)
diorite
tonalitic vein
diorite
5 mm

Figure 4

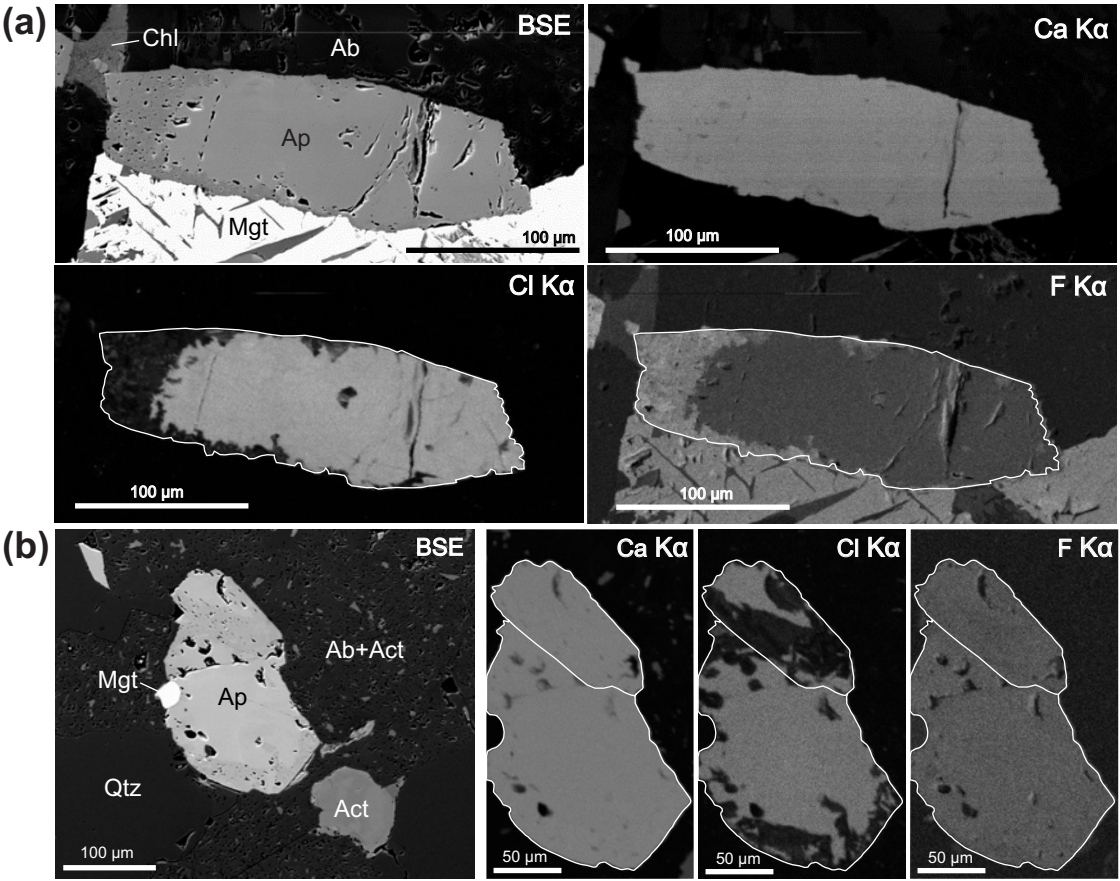
(a)
BSE
Chl
Ab
Ap
Mgt
100 µm
Ca Kα
100 µm
Cl Kα
100 µm
F Kα
100 µm
(b)
BSE
Ab+Act
Mgt
Ap
Qtz
Act
100 µm
Ca Kα
50 µm
Cl Kα
50 µm
F Kα
50 µm

Figure 5

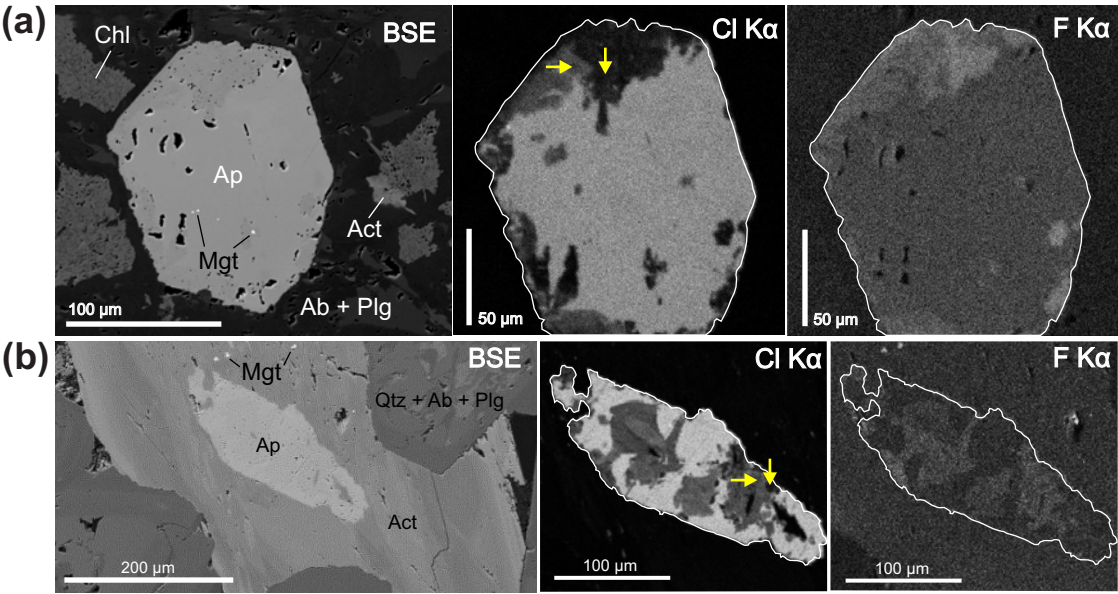
(a)
Chl
BSE
Ap
Act
Mgt
100 µm
Ab + Plg
Cl Kα
50 µm
F Kα
50 µm
(b)
Mgt
BSE
Qtz + Ab + Plg
Ap
Act
200 µm
Cl Kα
100 µm
F Kα
100 µm

Figure 6

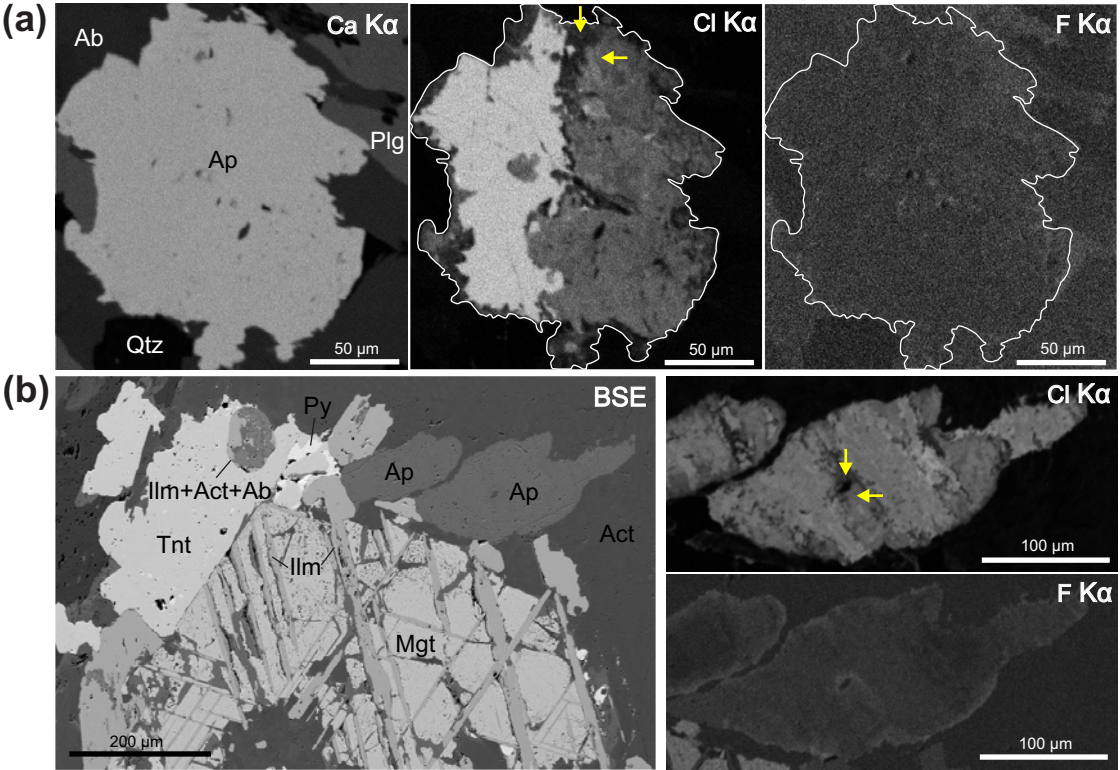
(a)
Ca Kα
Ab
Plg
Ap
Qtz
50 μm
Cl Kα
50 μm
F Kα
50 μm
(b)
BSE
Py
Ilm+Act+Ab
Ap
Ap
Act
Tnt
Ilm
Mgt
200 μm
Cl Kα
100 μm
F Kα
100 μm

Figure 7

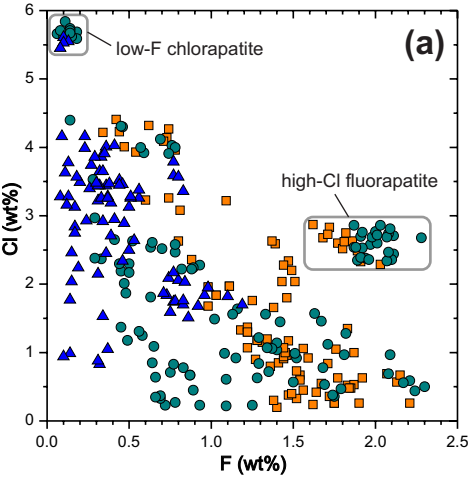
(a)
low-F chlorapatite
high-Cl fluorapatite
Cl (wt%)
F (wt%)
0
1
2
3
4
5
6
0.0
0.5
1.0
1.5
2.0
2.5

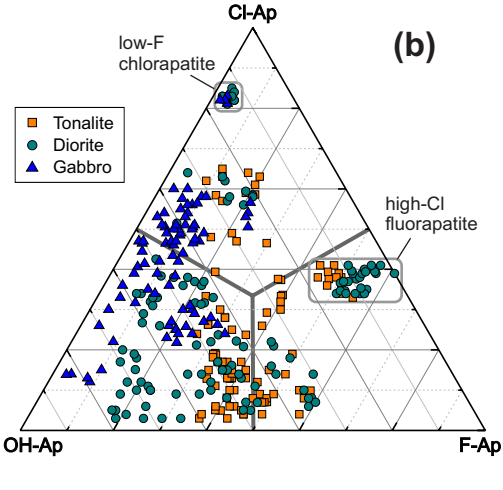
Cl-Ap
low-F
chlorapatite
(b)
Tonalite
Diorite
Gabbro
high-Cl
fluorapatite
OH-Ap
F-Ap

Figure 8

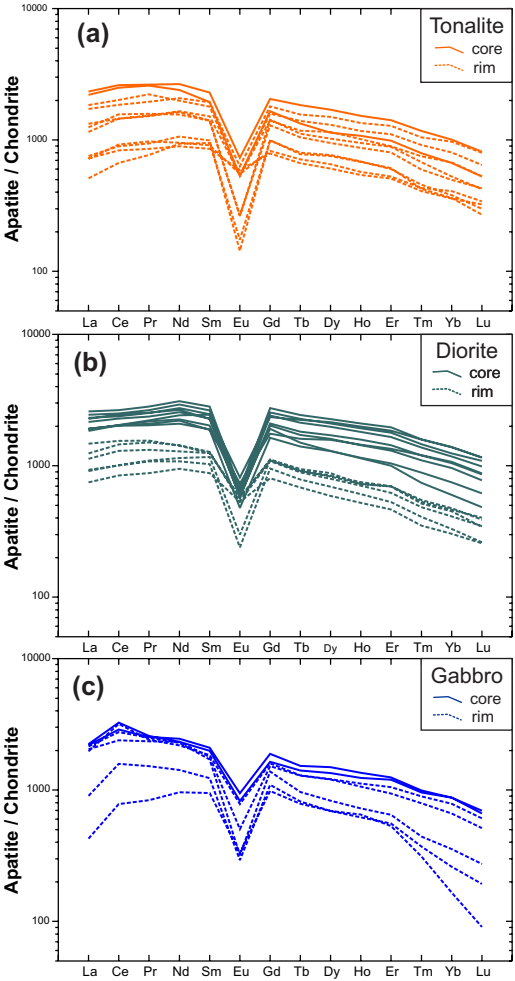
(a)
Tonalite
core
rim
(b)
Diorite
core
rim
(c)
Gabbro
core
rim
Apatite / Chondrite
10000
1000
100
La Ce Pr Nd Sm Eu Gd Tb Dy Ho Er Tm Yb Lu

Figure 9

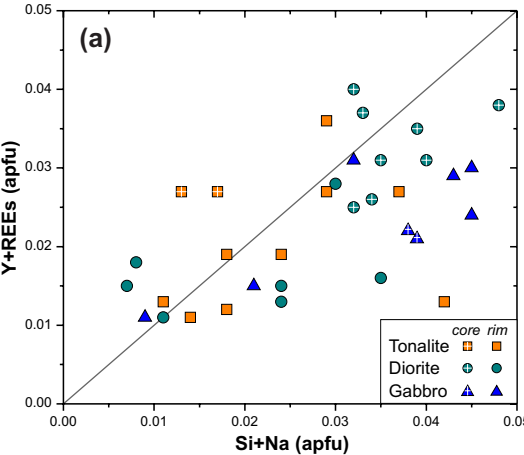
(a)
Y+REEs (apfu)
Si+Na (apfu)
0.00
0.01
0.02
0.03
0.04
0.05
core rim
Tonalite
Diorite
Gabbro

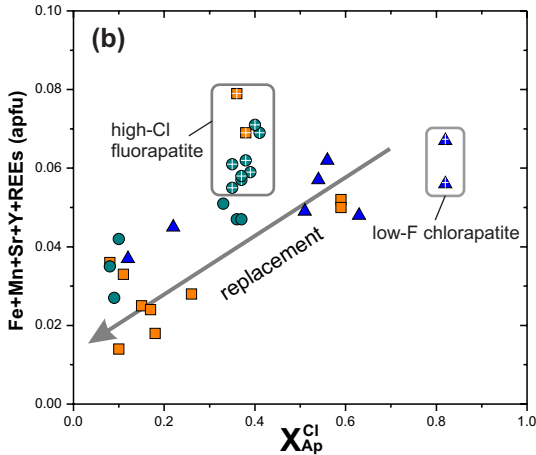
(b)
Fe+Mn+Sr+Y+REEs (apfu)
0.00
0.02
0.04
0.06
0.08
0.10
high-Cl
fluorapatite
low-F chlorapatite
replacement
0.0
0.2
0.4
0.6
0.8
1.0
X Cl Ap

Figure 10

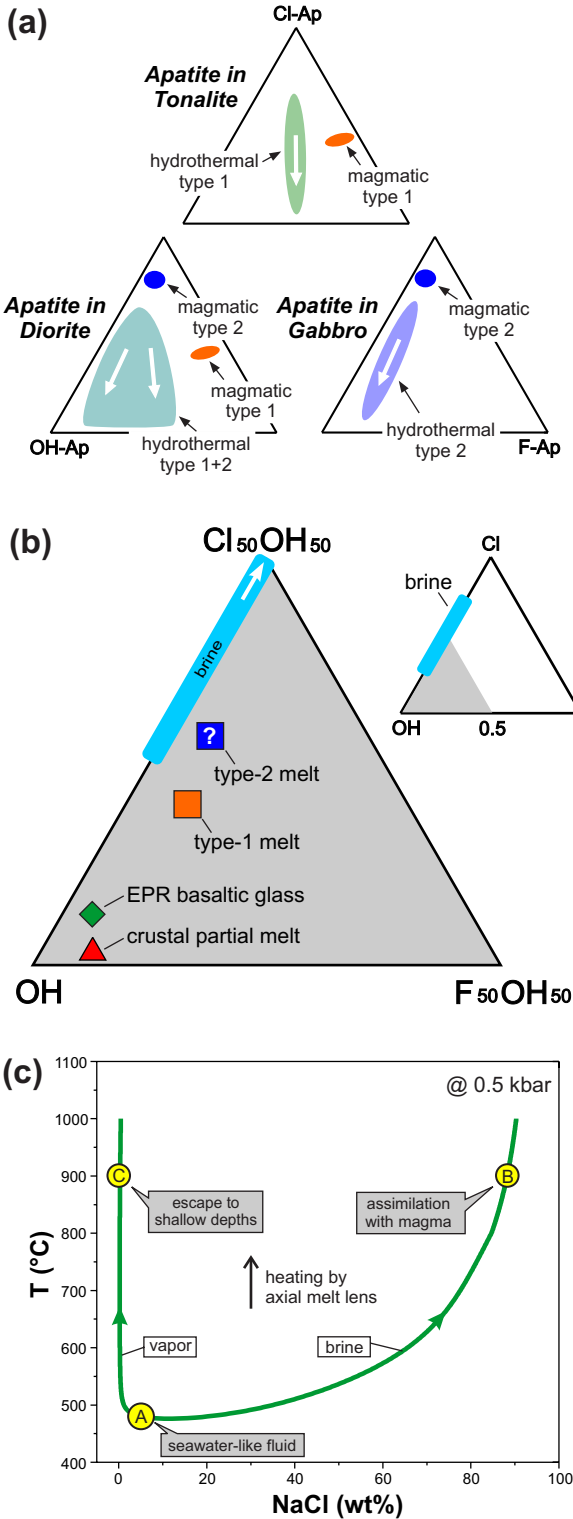
(a)
Cl-Ap
Apatite in Tonalite
hydrothermal type 1
magmatic type 1
Apatite in Diorite
magmatic type 2
magmatic type 1
hydrothermal type 1+2
OH-Ap
Apatite in Gabbro
magmatic type 2
hydrothermal type 2
F-Ap
(b)
Cl 50 OH 50
brine
?
type-2 melt
type-1 melt
EPR basaltic glass
crustal partial melt
OH
F 50 OH 50
Cl
brine
OH
0.5
F
(c)
@ 0.5 kbar
C
B
A
escape to shallow depths
assimilation with magma
heating by axial melt lens
vapor
brine
seawater-like fluid
T (°C)
NaCl (wt%)
1100
1000
900
800
700
600
500
400
0
20
40
60
80
100